Determination of the binding sites of the proton transfer inhibitors Cd^{2+} and Zn^{2+} in bacterial reaction centers

H. L. Axelrod, E. C. Abresch, M. L. Paddock, M. Y. Okamura, and G. Feher*

Department of Physics 0319, 9500 Gilman Drive, University of California at San Diego, La Jolla, CA 92093

Contributed by George Feher, December 2, 1999

The reaction center (RC) from *Rhodobacter sphaeroides* couples light-driven electron transfer to protonation of a bound quinone acceptor molecule, Q_B, within the RC. The binding of Cd^{2+} or Zn^{2+} has been previously shown to inhibit the rate of reduction and protonation of Q_B. We report here on the metal binding site, determined by x-ray diffraction at 2.5-Å resolution, obtained from RC crystals that were soaked in the presence of the metal. The structures were refined to *R* factors of 23% and 24% for the Cd^{2+} and Zn^{2+} complexes, respectively. Both metals bind to the same location, coordinating to Asp-H124, His-H126, and His-H128. The rate of electron transfer from Q_A^- to Q_B was measured in the Cd^{2+}-soaked crystal and found to be the same as in solution in the presence of Cd^{2+}. In addition to the changes in the kinetics, a structural effect of Cd^{2+} on Glu-H173 was observed. This residue was well resolved in the x-ray structure—i.e., ordered—with Cd^{2+} bound to the RC, in contrast to its disordered state in the absence of Cd^{2+}, which suggests that the mobility of Glu-H173 plays an important role in the rate of reduction of Q_B. The position of the Cd^{2+} and Zn^{2+} localizes the proton entry into the RC near Asp-H124, His-H126, and His-H128. Based on the location of the metal, likely pathways of proton transfer from the aqueous surface to $Q_B^{\cdot-}$ are proposed.

bacterial photosynthesis | *Rhodobacter sphaeroides* | metal ion binding | cation binding | x-ray crystallography

In the photosynthetic bacterium *Rhodobacter* (*Rb.*) *sphaeroides*, a 100-kDa integral membrane pigment–protein complex called the reaction center (RC) performs the initial light-driven electron and proton transfer reactions leading to the formation of a proton gradient across the bacterial membrane (1–3). The three-dimensional atomic structure of the RC from *Rb. sphaeroides* is known (4–7), and the functions of several key amino acid residues and cofactors have been established (1–3). The RC is composed of three protein subunits (L, M, and H) and a number of bound cofactors. Light drives the transfer of an electron from the primary donor of the RC, a bacteriochlorophyll dimer (D) through an intermediate acceptor, a bacteriopheophytin (ϕ_A), to the primary acceptor, a tightly bound ubiquinone molecule (Q_A). From $Q_A^{\cdot-}$, the electron is transferred to a loosely bound secondary quinone acceptor, Q_B. An exogenous cytochrome c_2 reduces D^+, thereby allowing a second electron to be transferred to Q_B. This transfer is coupled with proton uptake and results in the formation of quinol, Q_BH_2, which serves as a mobile carrier of protons to the cytochrome bc_1 complex (8–10). Cytochrome bc_1 oxidizes quinol and mediates proton transfer across the membrane.

The proton transfer pathways in the RC have been investigated by kinetic optical spectroscopy, site-directed mutagenesis, and x-ray crystallography. In the vicinity of Q_B, Ser-L223 (11), Glu-L212 (12, 13), and Asp-L213 (14, 15) have been shown to be critical residues for proton transfer to $Q_B^{\cdot-}$. Guided by the x-ray crystal structure, three possible pathways for proton transfer, consisting of a chain of protonatable groups (16, 17) from the cytoplasmic surface to Q_B, were postulated (6, 7, 18, 19), each having different entry points for the protons.

The recent finding that the stoichiometric binding of Cd^{2+} or Zn^{2+} to the RC decreased the rate of proton transfer to reduced Q_B $\geq$100-fold suggests that the physiological proton transfer occurs through a single pathway that is inhibited by the bound metal ion (20). Here we report on the localization, through x-ray crystallography, of the bound Cd^{2+} and Zn^{2+}, thereby identifying the region of proton entry and the dominant proton transfer pathway(s) leading from the surface of the RC to $Q_B^{\cdot-}$.

Experimental Procedures

Purification of RCs. RCs from *Rb. sphaeroides* were isolated in buffer containing 15 mM Tris·HCl at pH 8.0, 0.025% lauryldimethylamine N-oxide (LDAO; Fluka), and 0.1 mM EDTA and purified from the R26 strain as described (21). The RCs were extensively dialyzed against 10 mM Tris·HCl, pH 8.0/0.1% LDAO to remove EDTA, and were concentrated to $\approx$20 mg/ml by using a 1-ml diethylaminoethyl (DEAE) Toyopearl 650M (Supelco) column.

Crystallization. Crystals of the RC were obtained by vapor diffusion (22) at 19°C in 35-μl sitting drops with 1-ml reservoirs in Cryschem type plates (Charles Supper, Natick, MA). The crystals belong to the tetragonal $P4_32_12$ space group as first reported by Allen (23). The unit cell dimensions are $a = b = 140.1$ Å and $c = 271.6$ Å (7); they contain two RC molecules in the asymmetric unit.

X-Ray Data Collection. X-ray data were collected on three different crystals, containing: (*i*) Cd^{2+} bound to the RC in the dark-adapted charge neutral state of the RC (DQ_AQ_B); (*ii*) Cd^{2+} bound to the RC in the light-adapted, charge-separated state ($D^+Q_AQ_B^{\cdot-}$); (*iii*) Zn^{2+} bound to the RC in the dark-adapted state. One day prior to data collection, crystals were soaked in mother liquor [15% (wt/vol) PEG 4000/30 mM Tris·HCl, pH 8.0/0.18% LDAO, 12% (wt/vol) heptanetriol/0.1 M NaCl] containing either $CdSO_4$ or $ZnSO_4$ at 10 mM. Crystals were mounted on nylon loops and plunged into liquid nitrogen as described (7, 24). To trap the RCs in the light-activated state, crystals were illuminated before cooling as described in ref. 7.

X-ray diffraction data were collected at the Stanford Synchrotron Radiation Laboratory on Beamline 9-1, using synchrotron

Abbreviations: RC, reaction center; D, primary donor; Q_A, primary quinone electron acceptor; $Q_A^{\cdot-}$ semiquinone intermediate of Q_A; Q_B, secondary quinone electron acceptor; $Q_B^{\cdot-}$, semiquinone intermediate of Q_B; LDAO, lauryldimethylamine N-oxide.

Data deposition: The atomic coordinates have been deposited in the Protein Data Bank, www.rcsb.org (PDB ID codes 1DS8 for the RC from *Rhodobacter sphaeroides* in the charge-neutral state with Cd^{2+}, 1DV3 for the charge-separated state with Cd^{2+}, and 1DV6 for the charge-neutral state with Zn^{2+}).

*To whom reprint requests should be addressed. E-mail: gfeher@ucsd.edu.

The publication costs of this article were defrayed in part by page charge payment. This article must therefore be hereby marked "*advertisement*" in accordance with 18 U.S.C. §1734 solely to indicate this fact.

Table 1. X-ray data collection and refinement statistics

	Cd^{2+}-DQ_AQ_B state (dark)	Cd^{2+}-$D^+Q_AQ_B^-$ state (light)	Zn^{2+}-DQ_AQ_B state (dark)
Data collection			
Maximum resolution, Å	2.49	2.49	2.49
Total observations (unique)	94,449 (13,013)	92,263 (12,363)	94,967 (12,576)
Redundancy*	3.9	3.9	3.9
Mean $I/\sigma(I)^\dagger$ (highest resolution shell)	8.8 (3.6)	7.0 (2.3)	7.0 (2.3)
$R_{sym}^\ddagger$ (highest resolution shell), %	6.5 (21.0)	8.9 (33.4)	8.1 (32.8)
Completeness§ (last shell), %	99.1 (94.9)	95.5 (88.4)	96.7 (89.0)
Refinement			
Resolution range, Å	50–2.50	50–2.50	50–2.50
Reflections	93,504	92,156	94,672
R factor,¶ %	22.7	22.6	23.8
R_{free},‖ %	25.7	25.2	26.5
Deviation from ideal bond lengths, Å	0.012	0.013	0.014
Deviation from ideal bond angles, °	1.7	1.6	1.7

*Ratio of the total number of reflections measured to the total number of unique reflections.
†$I/\sigma(I)$ is the ratio of the average of the diffraction intensities to the average background intensity.
‡$R_{sym} = \Sigma_{hkl}\Sigma_j|I_{hkl} - \langle I_{hkl}\rangle|/\Sigma_{hkl}\Sigma_j|I_{hkl}|$, where $\langle I_{hkl}\rangle$ is the average intensity for a set of j symmetry-related reflections and I_{hkl} is the value of the intensity for a single reflection within a set of symmetry-related reflections.
§Completeness is the ratio of the number of reflections measured to the total number of possible reflections.
¶R factor $= (\Sigma_{hkl}|F_o| - |F_c|)/\Sigma_{hkl}|F_o|$ where $|F_o|$ is the observed structure factor amplitude and $|F_c|$ is the calculated structure factor amplitude.
‖$R_{free} = (\Sigma_{hkl,T}|F_o| - |F_c|)/\Sigma_{hkl,T}|F_o|$, where a test set, T (5% of the data), is omitted from the refinement.

radiation at a wavelength of 0.98 Å. During data collection, the crystal was cooled to ≈100 K with a stream of liquid nitrogen. To minimize overlap of reflections, crystals were oriented with the longest (c) axis along the rotation axis of the goniostat. X-ray reflections were recorded in 0.5° increments until more than 45° of data had been collected. Diffraction data were recorded on a Mar345 x-ray imaging plate (X-ray Research, Hamburg, Germany). For the determination of crystal orientation and the integration of reflection intensity, the MOSFLM (25) software package was used. The CCP4 (Collaborative Computational Project Number 4) (26) crystallographic software package was used to reduce the x-ray diffraction intensities to structure factor amplitudes. The data processing statistics are shown in Table 1.

X-Ray Refinement. The coordinates of the RC in the dark-adapted state [Protein Data Bank entry 1AIJ (7, 27)] were used as a starting model for the refinement of the Cd^{2+}- and Zn^{2+}-containing structures. Water and detergent molecules were omitted from the starting model. In the later stages of the refinement, water molecules were added into $|F_o| - |F_c|$ difference electron density peaks that were at least 3σ above the background level of the map and were within 4 Å of hydrogen bonding acceptor or donor atoms, using the CCP4 programs PEAKMAX and WATERPEAK (26). Rigid-body, positional, and isotropic temperature factor refinement of the starting model were carried out for each data set by using the CNS (28) software package with a maximum-likelihood refinement target function (29, 30) and noncrystallographic symmetry restraints. During the refinement, the metal-to-ligand distances were constrained to 2.30 Å for Cd^{2+} and 2.15 Å for Zn^{2+}. These distances correspond to the mean metal-to-ligand distances summarized in a recent survey (31). Electron density maps with coefficients $2|F_o| - |F_c|$ and $|F_o| - |F_c|$ were computed with the CCP4 (26) software package. The maps were contoured with the program MAPMAN (32) and displayed on a Silicon Graphics Indy R5000 Workstation with the program TOM-FRODO (33). The refined coordinates of the dark-adapted structure with Cd^{2+} were used as a starting model for the refinement of the light-activated state of the RC with Cd^{2+}. To reduce phase bias, the coordinates of both Cd^{2+} and Q_B were removed from the starting model prior to the refinement of the light-activated state.

Measurements of Electron Transfer Kinetics in Crystals. A microspectrophotometer of local design (34, 35) was used to measure the electron transfer rate from Q_A^- to Q_B ($k_{AB}^{(1)}$) in RC crystals. To increase the occupancy of Q_B in the crystals, 1 mM ubiquinone-4 (Sigma) was added to the mother liquor. To measure the effect of the bound metal ion on the electron transfer rate, 10 mM $CdSO_4$ was added to the mother liquor. To remove Cd^{2+} from the RC crystals, they were washed with mother liquor containing 10 mM EDTA.

Charge separation in RCs was accomplished with a single pulse of a PhaseR DL2100c laser (λ = 590 nm, 0.2 J per pulse, 0.4-μs pulsewidth at half maximum), directed onto the RC crystal that was placed between two sealed glass coverslips. After the laser flash, the absorbance at 460 nm (36, 37) was monitored by using a Bausch and Lomb xenon lamp to provide a high-intensity measuring beam. To improve the signal-to-noise ratio, 40 traces were averaged. Data were analyzed by using commercial software (Jandel PEAKFIT).

Results

Structure of the Metal Ion Complexes in the Dark-Adapted (DQ_AQ_B) State. The structures of the RC from *Rb. sphaeroides* with bound Cd^{2+} and Zn^{2+} were determined in the dark-adapted (DQ_AQ_B) state. Examination of the $|F_o| - |F_c|$ difference electron density maps, after rigid-body refinement, revealed the existence of a large difference density peak, 25σ above the background level in the Cd^{2+}-containing crystal and 10σ above background for the Zn^{2+}-containing crystal. This observation suggests a high occupancy of the binding sites. Cd^{2+} and Zn^{2+} bind at the same location. The metal ion site is located ≈20 Å from the Q_B site at the cytoplasmic surface of the RC (see Fig. 1). Adjacent to the peak and within coordination distance are the imidazole side chains of two histidines (His-H126 and His-H128) and the side chain of an aspartic acid (Asp-H124). For both metal complexes, the height of the electron density peaks and the location of the ligands, which are commonly found in metalloproteins, are consistent with the assignment of the peaks to a bound metal ion.

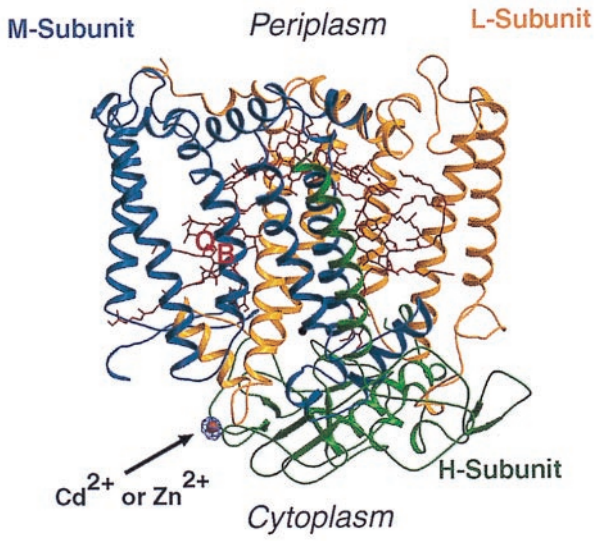

Fig. 1. Structure of the RC from *Rb. sphaeroides,* showing the location of the Cd^{2+} and Zn^{2+} binding sites (orange), L subunit (yellow), M subunit (blue), H subunit (green), and cofactors (red) with Q_B labeled. Difference electron density ($|F_o| - |F_c|$) contoured at 10σ above the mean value of the map is shown in purple surrounding Cd^{2+}. Illustration made with the programs BOBSCRIPT (38) and RASTER3D (39).

The metal ions were modeled into difference density peaks, and further refinement at a resolution 2.5 Å was carried out.

The most significant structural difference between the RC with and without a bound metal ion is the positions of the side-chain ligands. Both His-H126 and His-H128 appear to undergo side-chain conformational changes that enable them to bind to the metal ions. Both histidines coordinate Cd^{2+} or Zn^{2+} at the N^{δ} atoms of the imidazole side chains (Fig. 2). To model a covalent bond to the metal, the imidazole of His-H126 had to be rotated about the C^{β}–C^{γ} axis. One of the oxygens of the side chain of Asp-H124 is also coordinated to the metal ions (Fig. 2). There are no significant conformational changes in the polypeptide backbone conformation.

Additional rounds of coordinate and isotropic temperature factor refinement for the metal complexes led to *R* factors of 23% (R_{free} = 26%) and 26% (R_{free} = 27%) for Cd^{2+} and Zn^{2+}, respectively (Table 1). A few other difference peaks were observed, but they were much smaller (≤⅓) than the height of the major density peak. These peaks could represent anion or detergent binding sites.

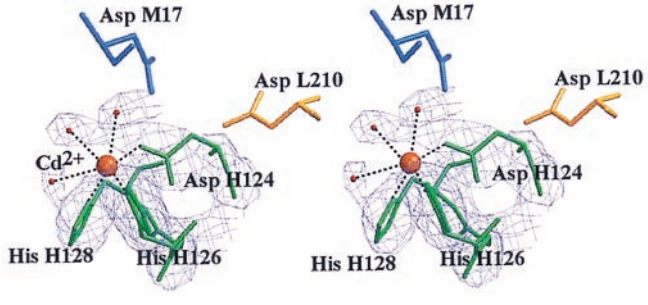

Fig. 2. Stereoview of the Cd^{2+} binding site (orange) on the RC from *Rb. sphaeroides*. The six Cd^{2+} ligands are His-H126, His-H128, Asp-H124 (green), and three water molecules (red). Two nearby aspartic acid residues, Asp-L210 (yellow) and Asp-M17 (blue), are part of a hydrogen bonding network that leads from the metal site to Q_B^- (see Fig. 5). $|F_o| - |F_c|$ difference electron density (purple) is contoured at 2.5σ and superimposed on the structure. To reduce phase bias, ligands were excluded in the calculation of the map.

From a least-squares overlap of the Cd^{2+} structure in the dark-adapted state with the native structure (7), a 0.4-Å root-mean-square deviation between all protein atoms in the two sets of coordinates was determined. This value is within experimental uncertainty of the coordinates. Thus, at our resolution, no additional differences between the dark-adapted structures, with and without the metal, could be discerned. Further comparison of the structures also shows that Q_B occupies the same position in RCs with and without a bound metal.

Subsequent stages of refinement revealed three difference electron density peaks (see Fig. 2) within 3 Å of the bound Cd^{2+}. These peaks were modeled as water molecules with the oxygen atoms coordinated to Cd^{2+}, at an average oxygen-to-metal distance of 2.7 ± 0.2 Å for the three water molecules. This distance is larger than 2.3 Å, the expected distance for strong coordination bonding between Cd^{2+} and oxygen ligands (31). The larger distances indicate that the water molecules are more weakly bound than the side-chain ligands. The bound water molecules and the side-chain ligands suggest an octahedral coordination geometry, which is commonly found in other metalloproteins containing Cd^{2+} (31).

An important difference between the Zn^{2+} and the Cd^{2+} structures is the coordination geometry of the metal site. The Zn^{2+} structure shows, in addition to the three amino acid residues, one water molecule, suggesting tetrahedral coordination, which is the predominant geometry found in Zn^{2+}-containing proteins (27, 31, 40).

Structure of the Cd^{2+} Complex in the Charge-Separated State. In native RCs, the transfer of the second electron to Q_B is coupled to the rapid protonation of the semiquinone intermediate Q_B^-. Consequently, knowledge of the structure of the RC–Cd^{2+} complex in the light-activated state (Cd^{2+}–$D^+Q_AQ_B^-$) may be important for understanding the mechanism of Cd^{2+} inhibition of proton transfer. We determined, therefore, the structure of the RC–Cd^{2+} complex in the light-activated state. The difference electron density maps revealed a peak, 20σ above background. This strong peak is at the same location and is within coordination distance to the same residues as in the dark structure.

The structure of the charge-separated state with Cd^{2+} has been refined at a resolution of 2.5 Å and an *R* factor of 23% (R_{free} = 25%) (Table 1). No significant changes in the structure of the side-chain ligands (His-H124, His-H126, and His-H128) are seen in the light-activated structure compared with the dark-adapted Cd^{2+} structure. At the present stage of refinement, electron densities corresponding to two water molecules as ligands were observed. The presence of one additional water ligand observed in the dark-adapted state may be attributed to the better quality of the x-ray diffraction data for the dark-adapted state (R_{sym} = 6.5%, Table 1) compared with the charge-separated state (R_{sym} = 8.9%) (Table 1).

The refined coordinates of the charge-separated state with Cd^{2+} overlap the native charge-separated coordinates without Cd^{2+} (PDB Entry 1AIG) (7) with a root-mean-square difference of 0.65 Å for all protein atoms. This is larger than the uncertainties in the coordinates, suggesting structural changes in the light-activated state of the RC upon Cd^{2+} binding. Examination of the structures with and without metal show no significant rearrangements of the polypeptide backbone. Therefore, we attribute the structural differences to side-chain rearrangements. A striking example of such a rearrangement is exhibited by Glu-H173. In light-activated structures of the RC without metal (see Fig. 3*b*), we observe weak electron density for the side chain of Glu-H173, which was reported by Stowell *et al.* (7), and was attributed to disorder. In the presence of Cd^{2+}, we observe

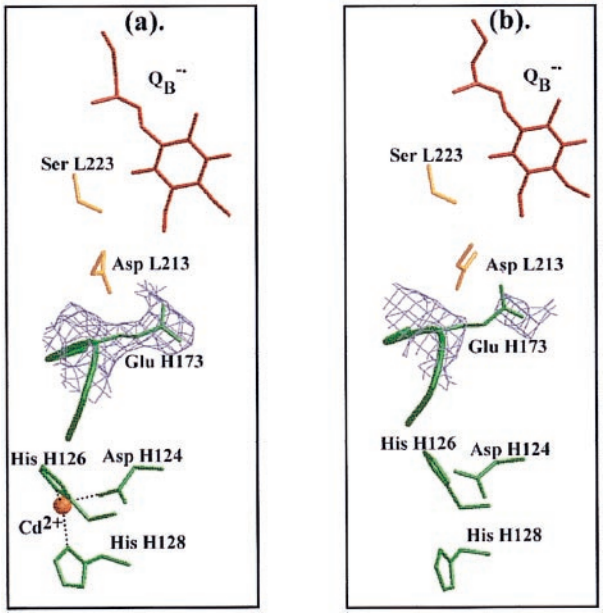

Fig. 3. $2|F_o| - |F_c|$ electron density map at Glu-H173 in the charge-separated state ($D^{+}Q_AQ_B^{-}$) of the RC from *Rb. sphaeroides* with Cd^{2+} (a) and without Cd^{2+} (*b*). The structure shown in *b* is similar to the one reported by Stowell *et al.* (7). Electron density contours (purple) are displayed at 1σ above the mean level of the map with the Glu-H173 side chain excluded for the calculation of phases. In the structure without Cd^{2+}, the electron density of the side chain of Glu-H173 is weaker, indicating greater mobility of the side chain, compared with the structure in the presence of Cd^{2+}.

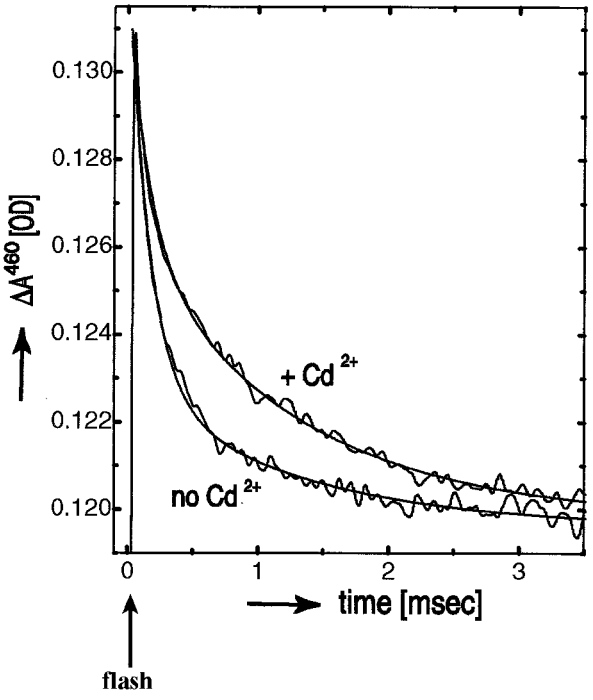

Fig. 4. Light-induced absorption changes at 460 nm after a laser flash in RC crystals with and without Cd^{2+}. Each trace is an average of 40 flashes. The absorbance change is associated with electron transfer from Q_A^{-} to Q_B ($Q_A^{-}Q_B \rightarrow Q_AQ_B^{-}$). Crystals were placed between two sealed coverslips in artificial mother liquor without and with 10 mM Cd^{2+}. The solid lines represent fits to a biexponential function with rate constants $k_1 = 6000\ s^{-1}$ and $k_2 = 800\ s^{-1}$. The rate constant and the increase in amplitude of the slower phase in the presence of Cd^{2+} are similar to those measured in solution (not shown), showing that the binding site in the crystal is the same as in solution.

strong electron density for the side chain of Glu-H173, indicating an ordered structure (see Fig. 3*a*). The implication of this structure for electron transfer is discussed in a later section. An additional finding is that the position of Q_B^{-} in the light structure with Cd^{2+} is the same as in RCs without Cd^{2+}.

Electron Transfer from Q_A^{-} to Q_B in RC Crystals. It was previously shown that in solution the binding of Cd^{2+} leads to a decrease in the rate of proton transfer and the rate of electron transfer from Q_A^{-} to Q_B (20, 41). We used the electron transfer kinetics as an assay to verify that the effect of Cd^{2+} in the crystal is the same as in solution.

The electron transfer rate was measured by monitoring the absorbance change at 460 nm after a laser flash (36, 37). The observed absorbance changes in RCs without and with Cd^{2+} are shown in Fig. 4. The solid lines represent fits to biexponential functions with rate constants of $k_1 = 6000\ s^{-1}$ and $k_2 = 800\ s^{-1}$. In the absence of Cd^{2+}, the faster phase predominates (80%). Upon addition of 10 mM Cd^{2+}, the amplitude of the slower phase increases to $\geq$50%. The rate constant as well as the changes in the amplitudes upon addition of Cd^{2+} are similar to those observed in solution. After the crystals had been washed with 10 mM EDTA to remove Cd^{2+}, the amplitude of the faster phase again predominated (data not shown).

Discussion

The Metal Binding Site. The binding of a single Cd^{2+} or Zn^{2+} cation to the RC decreases the rate of electron and proton transfer to reduced Q_B (20). The x-ray crystal structures reported here show one dominant Cd^{2+} or Zn^{2+} binding site on the RC. Both Cd^{2+} and Zn^{2+} bind at the same location, consistent with the competitive binding results found in solution (20). To test whether the metal ion-binding site is the same as that in solution, the kinetics of $k_{AB}^{(1)}$ ($Q_A^{-}Q_B \rightarrow Q_AQ_B^{-}$) in the crystal were measured. The observed kinetics in the presence and absence of Cd^{2+} were the same within experimental error as those measured in solution, indicating that the crystallographic site is the same as found in solution. Three residues on the H subunit (Asp-H124, His-H126, and His-H128) and three water molecules form ligands to Cd^{2+}. The location of the binding site of the metal inhibitors suggests an important role for the H subunit in proton transfer to Q_B^{-}. The x-ray crystal structures with Cd^{2+} and Zn^{2+} show no structural changes at the Q_B site, which is consistent with the relatively long distance ($\approx$20 Å) between the two sites.

Effect of Metal Binding on Protein Dynamics. It has been previously reported that Cd^{2+} or Zn^{2+} binding decreases the rate of the first electron transfer, $k_{AB}^{(1)}$, to Q_B ($DQ_A^{-}Q_B \rightarrow DQ_AQ_B^{-}$) (20, 41). Utschig *et al.* (41) attributed the decreased rate to a change in the dynamics of a conformational change. Independent evidence also suggests that $k_{AB}^{(1)}$ is limited by a conformational change (37, 42, 43). The challenge is to determine the molecular details of the conformational change. These can be obtained by comparing the RC structures with and without Cd^{2+}. The most conspicuous difference is the increased electron density of the Glu-H173 side chain (Fig. 3*a*), indicating that it is more ordered, hence less mobile. We therefore suggest that the mobility of the side chain of Glu-H173 plays an important role in the conformationally gated step (37) that determines the rate of transfer of the first electron to Q_B.

Proton Transfer Pathways. A dramatic effect of metal ion binding to the RC is a $\geq$100-fold reduction in the proton transfer rate (20). The x-ray structures of the RC–metal ion complexes show

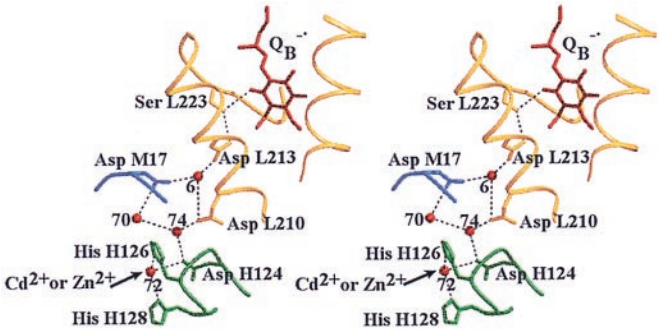

Fig. 5. Stereo representation of hydrogen bonding networks in the charge-separated ($D^+Q_AQ_B^-$) state of the native RC (7, 18) from *Rb. sphaeroides* spanning the region between the Cd^{2+} (or Zn^{2+}) binding site (indicated by arrow) and Q_B^-. L subunit (yellow), M subunit (blue), and H subunit (green), and Q_B^- and water molecules (red). Dashed lines represent hydrogen bonds. Wat-72 is displaced when Cd^{2+} or Zn^{2+} binds. The metal ion is located at the proton entry point. The hydrogen bonded networks form possible proton transfer pathways leading from the metal surface to Q_B^-

no change in the structure near the Q_B site. Consequently the effect of metal ion must be associated with changes in the vicinity of the binding site. The simplest explanation of the inhibitory effect of the metals on the proton transfer rate is that the metal impedes entry of protons into the RC (20). Thus, the position of the bound metal ion localizes the proton entry to a region of the H subunit near Asp-H124, His-H126, and His-H128.

The possible pathways connecting the metal binding site with Q_B are shown by dashed lines in Fig. 5. They include water molecules (Wat-70, Wat-74, and Wat-6), Asp-L210, Asp-L213, Asp-M17, and Ser-L223. These pathways are structurally close to the one previously proposed by Abresch *et al.* (18). The importance of Asp-L213 and Ser-L223 for proton transfer has been previously established (11, 14, 15) and that of Asp-L210 and Asp-M17 has been established by site-directed mutagenesis as discussed by Paddock *et al.* in the following paper (44).

Comparisons with Other Systems. All residues shown in Fig. 5 are conserved in the RC of a related bacterium, *Rhodobacter capsulatus* (45). We expect therefore, a similar effect of metal ion binding on proton transfer. In another related bacterium, *Rhodopseudomonas (Rps.) viridis* (46, 47), His-H126 and His-H128 are not conserved. However, an analogous acid–His pair (Glu-L210 and His-H178) may provide an alternate metal binding site in *Rps. viridis*.

Proton transfer pathways have been proposed for other bioenergetic membrane–protein complexes such as cytochrome *c* oxidase (48, 49) and bacteriorhodopsin (50, 51). Link *et al.* (52) reported that binding of Zn^{2+} to cytochrome bc_1 blocks protonation of a group near the hydroquinone oxidation site (53, 54). These pathways may share features with the pathway in *Rb. sphaeroides* discussed in this work.

Note Added in Proof. The binding sites of two additional proton transfer inhibitors, Ni^{2+} and Co^{2+}, were determined by x-ray diffraction analysis. They bind to Asp-M17 and His-H126, near the location of Wat-70 (see Fig. 5).

We thank the staff at the Stanford Synchrotron Radiation Laboratory (SSRL): A. Cohen, P. Ellis, M. Soltis, P. Kuhn, and T. McPhillips; A. Yeh for helping with the data collection; and D. Rees for helpful discussions. We thank R. Isaacson for his expert technical support in designing and running the microspectrophotometer. This work has been supported by National Institutes of Health Grant GM13191 and National Science Foundation Grant MCB 94–16652. This work is based on research conducted at SSRL, which is funded by the Department of Energy, Office of Basic Energy Sciences. The SSRL Biotechnology Program is supported by the National Institutes of Health, National Center for Research Resources, Biomedical Technology Program, and the Department of Energy, Office of Biological and Environmental Research.

1. Feher, G., Allen, J. P., Okamura, M. Y. & Rees, D. C. (1989) *Nature (London)* **339,** 111–116.
2. Michel-Beyerle, M.-E., ed. (1996) *Reaction Center of Photosynthetic Bacteria: Structure and Dynamics* (Springer, Berlin).
3. Breton, J., Nabedryk, E. & Vermeglio, A., eds. (1998) *Photosynth. Res.* **55,** 117–378.
4. Chang, C. H., Tiede, D., Tang, J., Smith, U., Norris, J. & Schiffer, M. (1986) *FEBS Lett.* **205,** 82–86.
5. Allen, J. P., Feher, G., Yeates, T. O., Komiya, H. & Rees, D. C. (1987) *Proc. Natl. Acad. Sci. USA* **84,** 6162–6166.
6. Ermler, U., Fritzsch, G., Buchanan, S. K. & Michel, H. (1994) *Structure* **2,** 925–936.
7. Stowell, M. H. B., McPhillips, T. M., Rees, D. C., Abresch, E. & Feher, G. (1997) *Science* **276,** 812–816.
8. Cramer, W. A. & Knaff, D. B. (1990) *Energy Transduction in Biological Membranes: A Textbook of Bioenergetics* (Springer, New York).
9. Gennis, R. B., Barquera, B., Hacker, B., VanDoren, S. R., Arnaud, S., Crofts, A. R., Davidson, E., Gray, K. A. & Daldal, F. (1993) *J. Bioenerg. Biomembr.* **25,** 195–209.
10. Crofts, A. R. & Berry, E. A. (1998) *Curr. Opin. Struct. Biol.* **8,** 501–509.
11. Paddock, M. L., McPherson, P. H., Feher, G. & Okamura, M. Y. (1990) *Proc. Natl. Acad. Sci. USA* **87,** 6803–6807.
12. Paddock, M. L., Rongey, S. H., Feher, G. & Okamura, M. Y. (1989) *Proc. Natl. Acad. Sci. USA* **86,** 6602–6606.
13. Takahashi, E. & Wraight, C. A. (1992) *Biochemistry* **31,** 855–866.
14. Takahashi, E. & Wraight, C. A. (1990) *Biochim. Biophys. Acta* **1020,** 107–111.
15. Paddock, M. L., Rongey, S. H., McPherson, P. H., Juth, A., Feher, G. & Okamura, M. Y. (1994) *Biochemistry* **33,** 734–745.
16. Nagle, J. F., Mille., M. & Morowitz, H. J. (1980) *J. Chem. Phys.* **72,** 3959–3976.
17. Okamura, M. Y. & Feher, G. (1995) in *Anoxygenic Photosynthetic Bacteria*, eds. Blankenship, R. E., Madigan, M. T. & Bauer, C. E. (Kluwer, Dordrecht, the Netherlands), pp. 577–594.
18. Abresch, E. C., Paddock, M. L., Stowell, M. H. B., McPhillips, T. M., Axelrod, H. L., Soltis, S. M., Rees, D. C., Okamura, M. Y. & Feher, G. (1998) *Photosynthesis Research* **55,** 119–125.
19. Fritzsch, G., Kampman, L., Kapaun, G. & Michel, H. (1998) *Photosynth. Res.* **55,** 127–132.
20. Paddock, M. L., Graige, M. S., Feher, G. & Okamura, M. Y. (1999) *Proc. Natl. Acad. Sci. USA* **96,** 6183–6188.
21. Isaacson, R. A., Lendzian, F., Abresch, E. C., Lubitz, W. & Feher, G. (1995) *Biophys. J.* **69,** 311–322.
22. McPherson, A. (1999) *Crystallization of Biological Macromolecules* (Cold Spring Harbor Lab. Press, Plainview, NY).
23. Allen, J. P. (1994) *Proteins Struct. Funct. Genet.* **20,** 283–286.
24. Rodgers, D. W. (1997) *Methods Enzymol.* **276,** 183–203.
25. Leslie, A. G. W. (1992) *Joint CCP4 and ESF-EACMB Newsletter on Protein Crystallography* (Daresbury Laboratory, Warrington, U.K.).
26. Bailey, S. (1994) *Acta Crystallogr. D* **50,** 760–763.
27. Bernstein, F. C., Koetzle, T. F., Williams, G. J., Meyer, E. E., Brice, M. D., Rodgers, J. R., Kennard, O., Shimanouchi, T. & Tasumi, M. (1977) *J. Mol. Biol.* **112,** 535–542.
28. Brünger, A. T., Adams, P. D., Clore, G. M., DeLano, W. L., Gros, P., Grosse-Kunstleve, R. W., Jiang, J. S., Kuszewski, J., Nilges, M., Pannu, N. S., *et al.* (1998) *Acta Crystallogr. D* **54,** 905–921.
29. Adams, P. D., Pannu, N. S., Read, R. J. & Brünger, A. T. (1997) *Proc Natl. Acad. Sci USA* **94,** 5018–5023.
30. Brünger, A. T., Adams, P. D. & Rice, L. M. (1998) *Curr. Opin. Struct. Biol.* **8,** 606–611.
31. Rulisek, L. & Vondrasek, J. (1998) *J. Inorg. Biochem.* **71,** 115–127.
32. Kleywegt, G. J. & Jones, T. A. (1996) *Acta Crystallogr. D* **52,** 826–828.
33. Jones, T. A. (1985) *Methods Enzymol.* **115,** 157–171.
34. Allen, J. P. & Feher, G. (1984) *Proc. Natl. Acad. Sci. USA* **81,** 4795–4799.
35. Adir, N., Axelrod, H. L., Beroza, P., Isaacson, R. A., Rongey, S. H., Okamura, M. Y. & Feher, G. (1996) *Biochemistry* **35,** 2535–2547.
36. Li, J., Gilroy, D., Tiede, D. M. & Gunner, M. R. (1998) *Biochemistry* **37,** 2818–2829.
37. Graige, M. S., Feher, G. & Okamura, M. Y. (1998) *Proc. Natl. Acad. Sci. USA* **95,** 11679–11684.
38. Esnouf, R. M. (1999) *Acta Crystallogr. D* **55,** 938–940.
39. Merritt, E. A. & Bacon, J. D. (1997) *Methods Enzymol.* **277,** 505–524.

40. Alberts, I. L., Nadassy, K. & Wodak, S. J. (1998) *Protein. Sci.* **7,** 1700–1716.
41. Utschig, L. M., Ohigashi, Y., Thurnauer, M. C. & Tiede, D. M. (1998) *Biochemistry* **37,** 8278–8281.
42. Tiede, D. M., Vazquez, J., Cordova, J. & Marone, P. A. (1996) *Biochemistry* **35,** 10763–10775.
43. Alexov, E. G. & Gunner, M. R. (1999) *Biochemistry* **38,** 8253–8270.
44. Paddock, M. L., Feher, G. & Okamura, M. Y. (2000) *Proc. Natl. Acad. Sci. USA* **97,** 1548–1553.
45. Williams, J. C., Steiner, L. A. & Feher, G. (1986) *Proteins* **1,** 312–325.
46. Michel, H., Weyer, K. A., Gruenberg, H. & Lottspeich, F. (1985) *EMBO J.* **4,** 1667–1672.
47. Deisenhofer, J., Epp, O., Miki, K., Huber, R. & Michel, H. (1984) *J. Mol. Biol.* **180,** 385–398.
48. Yoshikawa, S., Shinzawa-Itoh, K., Nakashima, R., Yaono, R., Yamashita, E., Inoue, N., Yao, M., Fei, M. J., Libeu, C. P., Mizushima, T., *et al*. (1998) *Science* **280,** 1723–1729.
49. Iwata, S., Ostermeier, C., Ludwig, B. & Michel, H. (1995) *Nature (London)* **376,** 660–669.
50. Luecke, H., Richter, H. T. & Lanyi, J. K. (1998) *Science* **280,** 1934–1937.
51. Luecke, H., Schobert, B., Richter, H. T., Cartailler, J. P. & Lanyi, J. K. (1999) *Science* **286,** 255–261.
52. Link, T. A. & von Jagow, G. (1995) *J. Biol. Chem.* **270,** 25001–25006.
53. Xia, D., Yu, C.-A., Kim, H., Xia, J.-Z., Kachurin, A. M., Zhang, L., Yu, L. & Deisenhofer, J. (1997) *Science* **277,** 60–66.
54. Crofts, A. R., Hong, S., Ugulava, N., Barquera, B., Gennis, R., Guergova-Kuras, M. & Berry, E. A. (1999) *Proc. Natl. Acad. Sci. USA* **96,** 10021–10026.